UC San Diego
UC San Diego Previously Published Works

Title

Neurodegeneration risk factor, EIF2AK3 (PERK), influences tau protein aggregation

Permalink

https://escholarship.org/uc/item/98r0v8r3

Journal

Journal of Biological Chemistry, 299(2)

ISSN

0021-9258

Authors

Park, Goonho
Xu, Ke
Chea, Leon
et al.

Publication Date

2023-02-01

DOI

10.1016/j.jbc.2022.102821

Peer reviewed

Neurodegeneration risk factor, *EIF2AK3* (PERK), influences tau protein aggregation

Goonho Park[1,2], Ke Xu[1], Leon Chea[1,2], Kyle Kim[1,2], Lance Safarta[2], Keon-Hyoung Song[1,2,3], Jian Wu[4], Soyoung Park[5], Hyejung Min[1], Nobuhiko Hiramatsu[1], Jaeseok Han[5], and Jonathan H. Lin[1,2,*]

From the [1]Department of Pathology, Stanford University, Palo Alto, California, USA; [2]VA Palo Alto Healthcare System, Palo Alto, California, USA; [3]Department of Pharmaceutical Engineering, Soonchunhyang University, Asan, Republic of Korea; [4]Department of Pharmacology, UC San Diego, La Jolla, California, USA; [5]Soonchunhyang Institute of Medi-bio Science (SIMS), Soonchunhyang University, Cheonan, Republic of Korea

Edited by Ursula Jakob

Tauopathies are neurodegenerative diseases caused by pathologic misfolded tau protein aggregation in the nervous system. Population studies implicate *EIF2AK3* (eukaryotic translation initiation factor 2 alpha kinase 3), better known as PERK (*protein kinase R-like endoplasmic reticulum kinase*), as a genetic risk factor in several tauopathies. PERK is a key regulator of intracellular proteostatic mechanisms—unfolded protein response and integrated stress response. Previous studies found that tauopathy-associated PERK variants encoded functional hypomorphs with reduced signaling *in vitro*. But, it remained unclear how altered PERK activity led to tauopathy. Here, we chemically or genetically modulated PERK signaling in cell culture models of tau aggregation and found that PERK pathway activation prevented tau aggregation, whereas inhibition exacerbated tau aggregation. In primary tauopathy patient brain tissues, we found that reduced PERK signaling correlated with increased tau neuropathology. We found that tauopathy-associated PERK variants targeted the endoplasmic reticulum luminal domain; and two of these variants damaged hydrogen bond formation. Our studies support that PERK activity protects against tau aggregation and pathology. This may explain why people carrying hypomorphic PERK variants have increased risk for developing tauopathies. Finally, our studies identify small-molecule augmentation of PERK signaling as an attractive therapeutic strategy to treat tauopathies by preventing tau pathology.

Tauopathies are age-related neurodegenerative diseases that include Alzheimer's disease (AD) and progressive supranuclear palsy (PSP) (1–4). Different brain regions are affected in these diseases that account for varying clinical presentations, but all tauopathies lead to progressive and irreparable morbidity that can quickly progress to mortality. In people, the microtubule-associated protein tau (*MAPT*) gene encodes tau protein and is abundantly transcribed throughout the brain (5–8). Alternative splicing of the *MAPT* transcript generates six tau protein isoforms that carry varying numbers of carboxy-terminal repeat (R) domains (5, 9, 10). In healthy cells, tau stabilizes and regulates microtubule assembly and is highly enriched in axons and also found in dendrites, nuclei, and extracellular space (5, 8, 11). By contrast, in tauopathies, tau adopts abnormal conformations, becomes hyperphosphorylated, and forms dense aggregates in neurons (2, 5, 7, 12). Environmental and genetic risk factors have been identified that influence tauopathy disease development and progression, but their pathomechanisms are incompletely understood (4).

EIF2AK3 (eukaryotic translation initiation factor 2 alpha kinase 3), more commonly known as PERK (*protein kinase R-like endoplasmic reticulum kinase*), is a genetic risk factor for tauopathies: PSP (13–15) and AD (16, 17). PERK is an important regulator of the unfolded protein response (UPR) and integrated stress response (ISR) (18–20). In response to endoplasmic reticulum (ER) stress protein misfolding, PERK slows cellular translation by phosphorylating eukaryotic initiation factor 2 alpha (eIF2α) (18). PERK signaling also initiates a characteristic transcriptional program through induction of transcription factors including activating transcription factor 4, which upregulates growth arrest and DNA damage–inducible protein 34 (GADD34) phosphatase, and CHOP (21–23). The GADD34 converts phosphorylated eIF2α (p-eIF2α) to eIF2α and thereby restores translation (24). $PERK^{-/-}$ mice develop marked endocrine and exocrine pancreatic cell death leading to diabetes mellitus (25), and this phenotype is closely recapitulated in Wolcott–Rallison syndrome (WRS), an autosomal recessive genetic disease caused by variants in human PERK (26, 27). Tauopathy symptoms are not features of WRS. Conversely, diabetes and/or pancreatic insufficiency are not primary features of tauopathies. It is unclear why PERK is linked with such markedly different human diseases.

Previously, we found that tauopathy-risk *PERK* variants showed reduced protein stability and signaling compared with protective *PERK* variants in cell culture assays (28). We also found that induced pluripotent stem cell–derived neurons from tauopathy patients showed reduced phosphorylation of eIF2α when challenged with ER stress–inducing chemicals (28). Based on these findings, we proposed that tauopathy-associated PERK variants are functional hypomorphs and that changes in PERK signaling somehow influence the

development of these neurodegenerative diseases. Here, we further evaluated the role of PERK in tauopathies, specifically focusing on the influence of PERK on tau protein aggregation. We performed structural modeling and bioinformatic analyses to analyze how tauopathy-associated *PERK* variants impact function. We evaluated how tau aggregation affected PERK signaling in a cell culture model and tested how chemical modulation of the PERK signaling pathway impacted tau aggregation. Last, we analyzed the status of PERK signaling and compared with tau neuropathology in AD brains. Our findings support that the PERK pathway prevents tau protein aggregation. Conversely, interfering with PERK pathway signaling increases tau aggregation.

Results

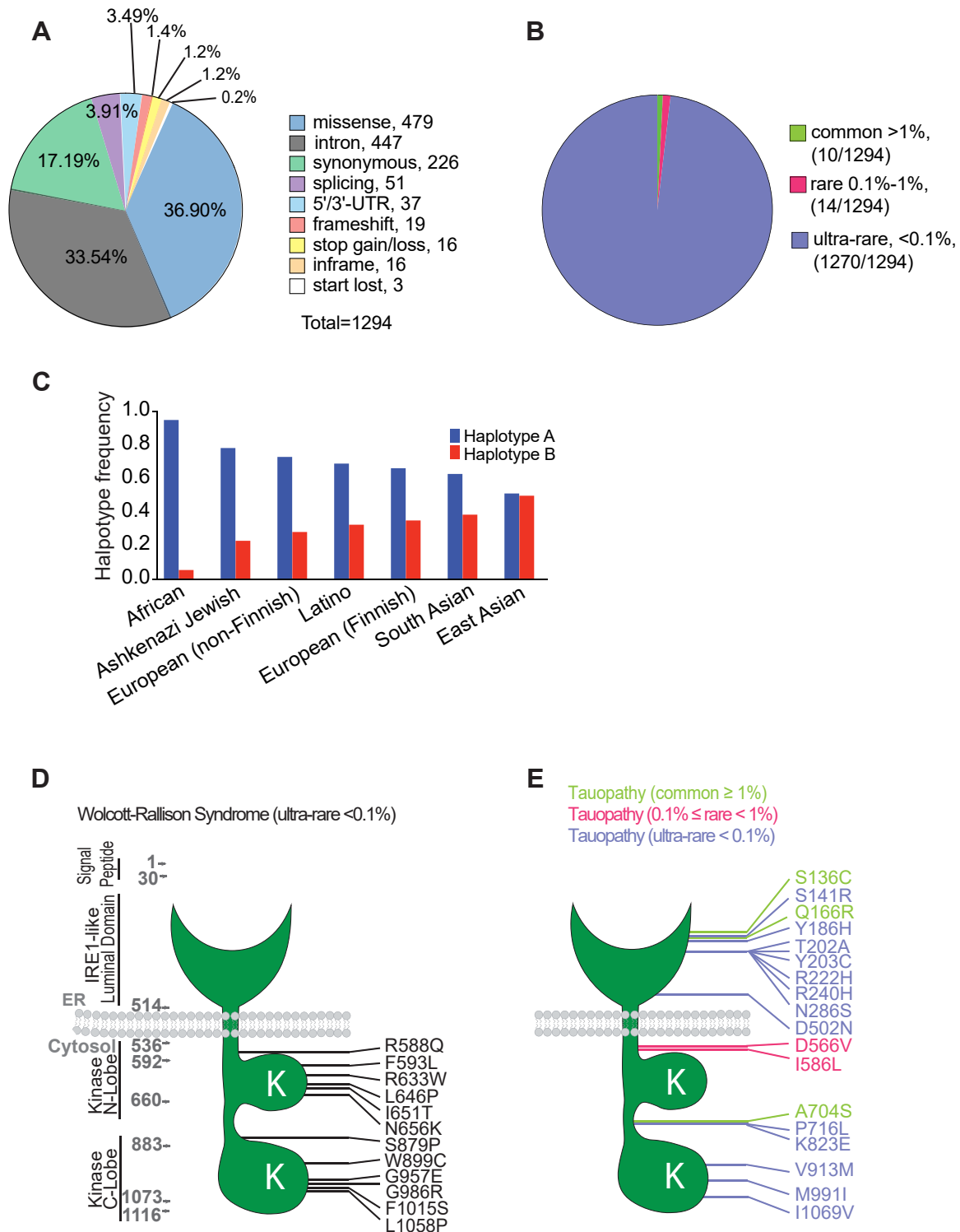### Population distribution of disease-associated PERK variants

Genetic studies identify PERK as a disease gene in WRS (26), PSP (13–15), and some forms of AD (16, 17). To gain insights into the association of PERK with such diverse diseases, we examined the distribution and molecular differences of PERK disease variants in the human population. We identified 1294 variants of human *EIF2AK3/PERK* in gnomAD database (gnomAD, version 2.1.1; Genome build: GRCh37/hg19; Ensembl gene: IDENSG00000172071.7) that introduced missense and nonsense changes in coding exons as well as targeted many noncoding regions (Fig. 1A and Data S1). Almost all variants (1270/1294) were ultrarare with allelic frequencies below 0.1% (Fig. 1B and Data S1). Fourteen variants were rare with allelic frequencies between 0.1% and 1% (Fig. 1B and Data S1). The remaining 10 *PERK* variants were common with >1% frequency (Fig. 1B and Data S1). WRS-associated *PERK* variants all arose at ultrarare frequencies and introduced nonsense (25 variants) or missense (12 variants) changes exclusively (Fig. 1D and Data S1) (27). By contrast, tauopathy-associated *PERK* variants included common, rare, and ultrarare variants that introduced missense changes or affected noncoding regions but did not cause nonsense changes (Fig. 1E and Data S1). Interestingly, the most common *PERK* variant, haplotype B (14, 29), originally identified as a tauopathy risk factor (13), showed striking differences in frequency between racial/ethnic groups (Fig. 1C and Data S2), ranging from 5% in African individuals to 49% in East Asian individuals. Conversely, the protective haplotype A *PERK* variant showed an inverse frequency in these populations (Fig. 1C and Data S2).

Next, we focused on the *PERK* variants that introduced missense changes in the protein. The human PERK protein is a 1116-amino acid type 1 integral membrane protein embedded in the ER with a luminal ER stress–sensing domain, coupled to a cytosolic kinase domain (18). The 12 missense variants linked to WRS all targeted the kinase domain (Fig. 1D). By contrast, the 10 tauopathy-associated missense variants targeted the ER stress–sensing luminal domain and less frequently affected cytosolic residues (Fig. 1E). No overlap was found between WRS and tauopathy-associated PERK variants.

These genetic observations suggest that disruption of PERK function underlies the pathogenesis of WRS. By contrast, in tauopathies, kinase function is preserved, but ER stress–sensing domain of PERK is altered.
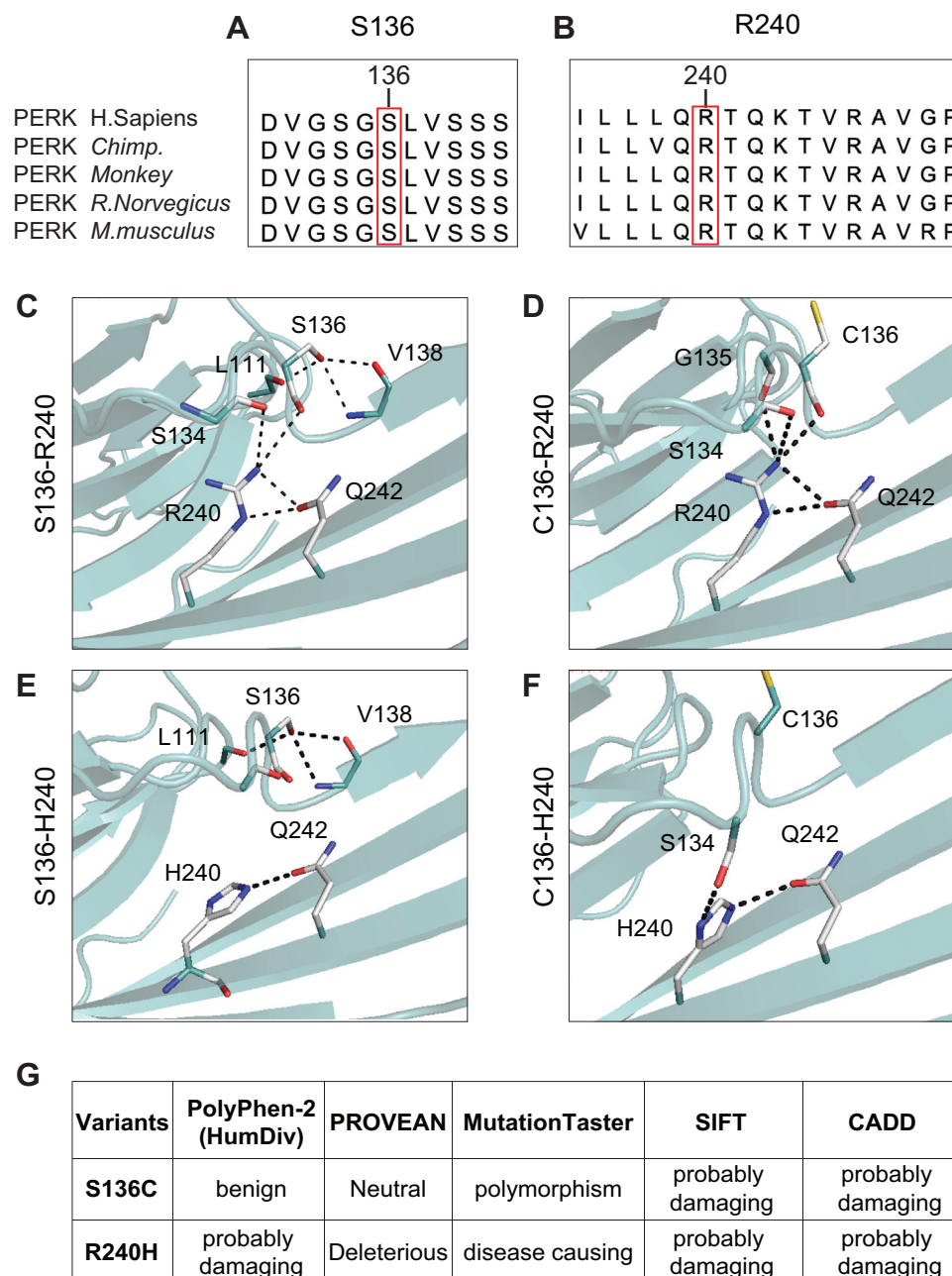
Tauopathy-associated PERK variants disrupt hydrogen bond formation in the ER stress–sensing luminal domain

High-resolution mouse and human PERK luminal domain crystal structures (30, 31) enable modeling of the impact of tauopathy-risk PERK luminal domain variants on the ER stress–sensing domain of PERK. We focused on two luminal domain residues, S136 and R240, because they are well conserved between mammalian PERK proteins (Fig. 2, A and B). A S136C conversion was present in the haplotype B PERK tauopathy risk variant (29), and an R240H conversion was found independently as a risk variant in AD cohorts (17). Neither of these amino acid substitutions are reported in other mammalian PERK proteins (Fig. 2, A and B). When we modeled the S136 and R240 residues onto the mammalian PERK luminal domain structure (Protein Data Bank [PDB] ID: 4YZY) using PyMol, we observed a direct hydrogen bond (H-bond) between S136 and R240 and six additional H-bond interactions formed by surrounding residues, L111, S134, V138, and Q242 (Fig. 2C). Structural modeling predicted that the combination of the C136 risk variant with the R240 protective variant was still able to form one direct H-bond, but only four H-bonds were formed by surrounding residues, S134, G135, and Q242 (Fig. 2D). The combination of the S136 protective variant with the H240 risk variant lost direct H-bond formation but retained four H-bonds between L111, S136, V138, and Q242 (Fig. 2E). Last, structural modeling predicted that the combination of a C136 risk variant and H240 risk variant was unable to form direct H-bonds, and only two H-bonds could form from surrounding residues, S134 and Q242 (Fig. 2F). In sum, structural modeling of these two human variants on the mammalian PERK luminal domain structure revealed a negative impact of disease-associated tauopathy conversions at the 136 and 240 residues upon H-bond formation. The protective variants generated seven potential H-bonds, but introduction of disease variants impaired H-bond formation between these two residues and the local structural environment. H-bonds stabilize tertiary PERK protein conformation (30). The functional consequences of loss of H-bonds on PERK's luminal domain ER stress–sensing properties are unclear. However, bioinformatic algorithms predict both conversions to be pathogenic (Fig. 2G). PolyPhen-2 (Polymorphism Phenotyping v2), PROVEAN (protein variation effect analyzer), MutationTaster, SIFT (sorting intolerant from tolerant), and combined annotation–dependent depletion (CADD) found R240H to be pathogenic; and the S136C conversion was pathogenic when analyzed by SIFT and CADD (Fig. 2G). Put together, these analyses support that tauopathy-associated PERK variants negatively impact the structure of the ER stress–sensing luminal domain with predicted pathologic consequences.

Figure 1. Molecular function and population distribution of PERK variants in human diseases. *A*, pie chart shows the molecular functional classification of 1294 genetic human *PERK* variants reported in Genome Aggregation Database (gnomAD). *B*, pie chart shows the frequency of human *PERK* variants reported in gnomAD. About 1270 *PERK* variants are ultrarare (<0.1% frequency). About 14 *PERK* variants are rare (0.1% to 1% frequency). About 10 variants are common (>1% frequency). *C*, prevalence of the two most common *PERK* variants, *haplotype A* and *haplotype B*, across seven racial/ethnic groups found in gnomAD. The frequency of tauopathy-risk variant, *haplotype B*, ranges from ∼49% in East Asian populations to ∼5% in African population. Conversely, the frequency of tauopathy-protective variant, *haplotype A*, ranges from 94% in African population to ∼50% in East Asian populations. *D* and *E*, PERK protein *cartoons* show positions of missense variants linked to WRS (*D*) and tauopathies (*E*) as reported in gnomAD database and NCBI since 2000. Functional domains of the 1116 amino acid human PERK protein include IRE1-like luminal ER stress–sensing domain, ER transmembrane domain, and amino (N) and carboxyl (C) kinase lobes in the cytoplasmic domain. PERK missense variants linked to WRS are all ultrarare and target PERK's N- and C- kinase lobes. PERK missense variants linked to tauopathies include common (*green*), rare (*red*), and ultrarare (*blue*) variants. Tauopathy PERK missense variants frequently map to PERK's luminal domain; do not overlap with WRS variants; and do not target the kinase lobes. ER, endoplasmic reticulum; IRE1, inositol-requiring enzyme 1; NCBI, National Center for Biotechnology Information; PERK, protein kinase R-like endoplasmic reticulum kinase; WRS, Wolcott–Rallison syndrome.

Figure 2. Tauopathy-associated variants disrupt hydrogen bonds in the PERK luminal domain. *A* and *B*, amino acid sequence alignments show conservation of human tauopathy protective PERK variants, S136 and R240, with chimpanzee, monkey, rat, and mouse PERK proteins. Human tauopathy PERK risk variants, C136 and H240, are not reported in other mammalian PERK proteins. *C–F*, hydrogen bonds formed by the PERK 136 and 240 residues were modeled by PyMol using the mouse PERK luminal domain crystal structure (PDB ID: 4YZY; MMDB ID: 129295). *C*, the combination of the protective PERK S136 and R240 variants forms seven H-bonds (*dashed lines*) locally including one direct S136-R240 H-bond. *D*, the combination of the risk PERK C136 and protective R240 variants forms five H-bonds locally including one direct C136-R240 H-bond. *E*, the combination of the protective PERK S136 and risk H240 variants forms four H-bonds locally. S136-H240 cannot form direct H-bonds. *F*, the combination of risk PERK C136 and H240 variants forms two H-bonds. C136-H240 cannot form direct H-bonds. *White* = carbon; *blue* = nitrogen; *red* = oxygen; and *yellow* = sulfur. *G*, pathogenicity of PERK S136C and R240H missense changes was bioinformatically assessed by five algorithms: PolyPhen-2 (HumDiv), PROVEAN, MutationTaster, SIFT, and CADD. PERK S136C was pathogenic using SIFT and CADD. PERK R240H was pathogenic in all algorithms. CADD, combined annotation–dependent depletion; MMDB, Molecular Modeling Database; PDB, Protein Data Bank; PERK, protein kinase R-like endoplasmic reticulum kinase; PolyPhen-2, protein kinase R-like endoplasmic reticulum kinase; PROVEAN, protein variation effect analyser; SIFT, sorting intolerant from tolerant.

Tau aggregation does not induce ER stress or ER stress–associated degradation and negatively impacts PERK- and inositol-requiring enzyme 1–mediated gene expression in vitro

Tau protein aggregation is a defining feature of tauopathies. We next examined how tau protein aggregation affects PERK signaling and related ER stress–induced processes. We turned to an *in vitro* human embryonic kidney 293 (HEK293) cell model of tau aggregation, "Biosensor" cells that stably express TauRD(P301S)-YFP at low levels diffusely in the cytosol (32–34). When transfected with tauopathy brain protein lysates, the TauRD(P301S)-YFP aggregates into distinct

fluorescent puncta (32–34). We prepared brain protein lysates from the PS19 tauopathy mouse model that expresses human P301S tau protein throughout the nervous system (35) and from wildtype mice (Fig. 3A). We confirmed abundant pathologic human tau protein in PS19 mice brain lysates that induced fluorescent tau aggregates when transfected into Biosensor cells (Fig. 3, A, C, and D), whereas wildtype mouse brain lysates showed none of these properties (Fig. 3, A, C, and D). We then examined the expression levels of a panel of 31 PERK-regulated genes during tau aggregation in this model using RNA-Seq. These genes were previously shown to be regulated by PERK (36, 37), and we also verified robust induction of these genes in thapsigargin-treated Biosensor cells (Fig. S1, A and B; Datas S3 and S4). When we examined PS19 brain lysate–treated Biosensor cells, we saw no induction, but instead, observed a small but significant reduction in expression of the PERK-regulated gene set (Fig. 3F, ****$p \leq 0.0001$, one-sample t test and two-tailed Wilcoxon signed rank test). Examination of five individual PERK-regulated genes, *ATF3*, *RELB*, *ASNS*, *GADD34*, and *GADD45A*, also showed reduction in expression in PS19 brain–treated cells *versus* controls (Fig. 3E, **$p \leq 0.01$, two-tailed Student's t test). Expression of the *PERK* gene itself was not changed in PS19 *versus* wildtype brain-treated cells (Fig. 3E). Next, we examined the status of inositol-requiring enzyme 1 (IRE1) and activating transcription factor 6 (ATF6) signaling in Biosensor cells during tau aggregation in our RNA-Seq datasets. For IRE1 signaling, we examined 32 genes previously demonstrated to be regulated by IRE1 (36, 38). We verified their robust induction in thapsigargin-treated Biosensor cells (Suppl. Fig. 1, C and D; Datas S3 and S4). When we examined PS19 brain lysate–treated cells, we also saw a significant reduction in expression of the IRE1-regulated gene set (Fig. 3H, ****$p \leq 0.0001$, one-sample t test and two-tailed Wilcoxon signed rank test). Examination of selected individual IRE1-target genes, *ERdj4*, *SLC3A2*, *VEGFA*, *UFM1*, confirmed significant reduction in gene expression (Fig. 3G, **$p \leq 0.01$, two-tailed Student's t test). *IRE1* gene expression itself was not changed (Fig. 3G). For ATF6 signaling, we examined expression of 74 genes previously reported to be induced by ATF6 (36, 39, 40) and also robustly upregulated in Biosensor cells after thapsigargin treatment (Fig. S1, E and F; Datas S3 and S4). By contrast to the PERK- and IRE1-gene panels, the ATF6-regulated genes showed no significant changes with PS19 brain treatment (Fig. 3, I and J). Last, we analyzed a 74 gene ER stress–associated degradation (ERAD) panel present in the Gene Ontology (GO) database ERAD term (GO:0036503) (http://amigo.geneontology.org/amigo/term/GO:0036503). As expected, we found significant induction of the ERAD gene set in Biosensor cells after thapsigargin treatment (Fig. S1G). By contrast, ERAD gene expression was not altered with PS19 brain treatment (Fig. 3, K and L). Bioinformatic pathway analysis on the entire RNA-Seq dataset using GO and gene set enrichment analysis (GSEA) further confirmed significant induction of ER stress and ERAD in thapsigargin-treated Biosensor cells (Figs. S1H and S2); whereas PS19 brain treatment did not induce ERAD, and ER stress was not changed by

GSEA and showed significant downregulation by GO analysis (Figs. 3L and S2). Consistent with these transcriptomic findings, we found pronounced increase in p-eIF2α levels in thapsigargin-treated Biosensor cells that was not seen in PS19 brain–treated lysates (Fig. S1I). In sum, these results demonstrate that tau aggregation does not trigger ER stress or ERAD in the Biosensor cell culture model. Instead, tau aggregation is associated with a small but significant downregulation of PERK-mediated gene expression.

Genetic and chemical inhibition of PERK pathway promotes tau aggregation

Our genetic RNA-Seq experiments in Biosensor cells identified a correlation between tau aggregation and reduced PERK signaling. To test for causality between PERK pathway signaling and tau aggregation, we added small molecules that target PERK, GADD34, or eIF2B to Biosensor cells undergoing tau aggregation. We used PERK inhibitors, GSK2656157, GSK2606414, or ISRIB, which locks eIF2B in an active state (41–43). To increase p-eIF2α levels, we added GADD34 inhibitor, salubrinal (44), to PS19 brain–transfected cell media. We found significant increase in tau fluorescent puncta with addition of GSK2656157, GSK2606414, or ISRIB, whereas salubrinal treatment significantly reduced the formation of fluorescent puncta (Fig. 4, A and B). Furthermore, we found that addition of salubrinal to PERK inhibitor GSK2606414-treated cells could antagonize the formation of the fluorescent tau aggregates (Fig. 4, C and D). These studies show that inhibition of PERK or locking eIF2B in an active state directly promotes tau aggregation, whereas increased eIF2α phosphorylation prevents tau aggregation in Biosensor cells.

To further test the relationship between PERK signaling and tau aggregation, we transduced TauRD(P301S)-YFP into *PERK*$^{+/+}$ and *PERK*$^{-/-}$ mouse embryonic fibroblasts (MEFs) (45). In *PERK*$^{+/+}$ MEFs, the fluorescence signal from the TauRD(P301S)-YFP construct was diffusely found in cell soma, whereas in *PERK*$^{-/-}$ MEFs, the fluorescent signal was found in intense puncta (Fig. 4E). When we examined protein lysates from these transduced *PERK* MEFs, we saw that TauRD(P301S)-YFP protein redistributed from the soluble fraction in *PERK*$^{+/+}$ MEFs to insoluble fraction in *PERK*$^{-/-}$ MEFs (Fig. 4F). Next, we transduced TauRD(P301S)-YFP into *eIF2α*$^{S/S}$ (wildtype) and *eIF2α*$^{A/A}$ (ablation of phosphorylation on 51 amino acid) MEFs (46). Similar to results seen in *PERK*$^{+/+}$ and *PERK*$^{-/-}$ MEFs, TauRD(P301S)-YFP fluorescence intensity was dramatically increased in *eIF2α*$^{A/A}$ MEFs as compared with *eIF2α*$^{S/S}$ MEFs (Fig. 4G) although puncta were less visible. Protein lysates from transduced *eIF2α*$^{S/S}$ and *eIF2α*$^{A/A}$ cells showed that TauRD(P301S)-YFP protein was increased in both soluble and insoluble fractions (Fig. 4H). Immunoblot analysis of eIF2α phosphorylation and PERK confirmed the absence of both proteins in *PERK*$^{-/-}$ and the absence of p-eIF2α in *eIF2α*$^{A/A}$ MEFs (Fig. 4, F and H). Taken together, these results support that increased eIF2 phosphorylation prevents tau aggregation *in vitro*, and that impaired PERK activity or loss of eIF2 phosphorylation increases tau aggregation.
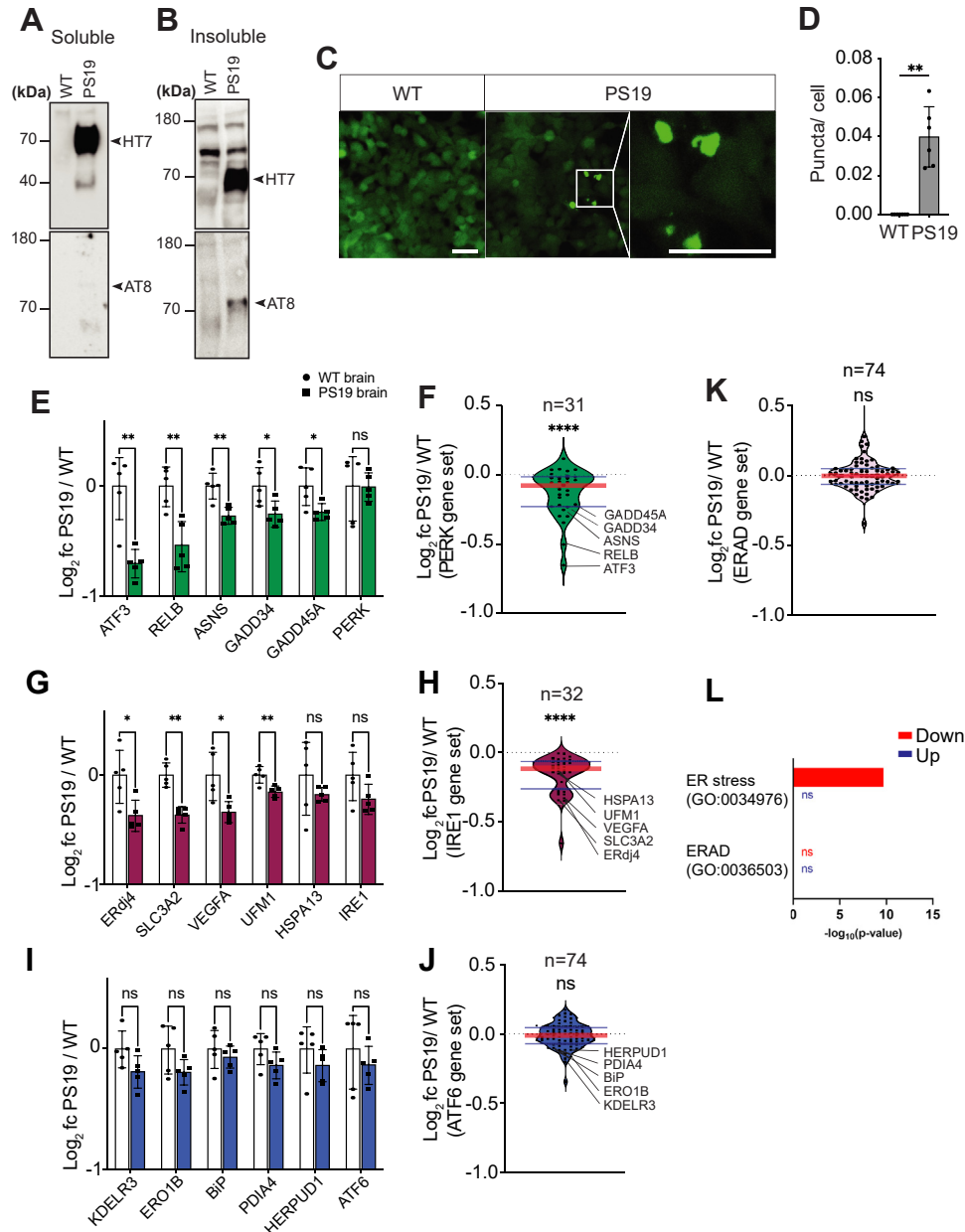
Figure 3. Tau aggregation in cell culture does not induce ER stress. *A* and *B*, protein lysates were prepared from wildtype and PS19 mouse brains. Soluble and insoluble protein lysate fractions were immunoblotted for total human Tau (HT7) and phospho-human Tau (AT8). *Arrowheads* mark positions of tau protein. *C*, Biosensor cells were transfected with wildtype or PS19 soluble brain lysate. After 24 h, Tau-YFP aggregates (puncta) were imaged by fluorescent microscopy. The *white box* outlines magnified image of Biosensor cells with puncta. The scale bar represents 50 μm. *D*, fluorescent puncta were quantified after wildtype or PS19 mouse brain lysate transfection, and the puncta number was normalized to cell number (**$p \leq 0.01$, one-tailed Student's t test, n = 6 independent transfections, mean ± SD). *E–I*, the mRNA levels of PERK-, IRE1-, ATF6-, and ERAD-regulated genes were examined by RNA-Seq of Biosensor cells transfected with wildtype or PS19 mouse brain protein lysate for 24 h. *E* and *F*, gene expression levels of 31 PERK-regulated genes in PS19 brain lysate–treated cells relative to wildtype brain lysate–treated cells are shown as $\log_2$ fold change. Graph I shows levels of the five PERK-regulated genes most significantly reduced between wildtype and PS19-treated cells and expression levels of the *PERK* gene itself. The violin plot (*F*) shows levels of the entire PERK-regulated gene set. *G* and *H*, gene expression changes of 32 IRE1-regulated genes in PS19-treated cells relative to wildtype treated are shown. The graph (*G*) shows levels of the five IRE1-regulated genes most differentially expressed between wildtype and PS19-treated cells and expression levels of *IRE1* gene itself. The violin plot (*H*) shows levels of the entire IRE1-regulated gene set. *I* and *J*, gene expression changes of 74 ATF6-regulated genes in PS19 brain lysate–treated cells relative to wildtype treated are shown. The graph (*I*) shows levels of the five ATF6-regulated genes most differentially expressed between wildtype and PS19-treated cells and expression levels of ATF6 gene itself. The violin plot (*J*) shows levels of the entire ATF6-regulated gene set. *K*, the violin plot shows levels of 74 ERAD-regulated genes. *L*, GO analysis identifies significantly decreased ER stress term (GO:0034976) in PS19-treated Biosensor cells. ERAD pathway (GO:0036593) shows no significant (ns) change after PS19 brain treatment. Error bars in *E*, *G*, and *I* represent mean ± SD. *Black circles* and *squares* represent five independent experimental replicates. (*$p \leq 0.05$, **$p \leq 0.01$, ns, two-tailed Student's t test). The *red horizontal line* in figures *F*, *H*, *J*, and *K* marks the median level of expression of the gene set, and the *thin horizontal blue lines* delimit upper and lower gene expression quartiles in the violin plots. (****$p \leq 0.0001$, one-sample t test and two-tailed Wilcoxon signed rank test, n = 5 experimental replicates). Detailed gene expression RNA-Seq information is shown in Data S3. ATF6, activating transcription factor 6; ER, endoplasmic reticulum; ERAD, ER stress–associated degradation; GO, Gene Ontology; IRE1, inositol-requiring enzyme 1; PERK, protein kinase R-like endoplasmic reticulum kinase.
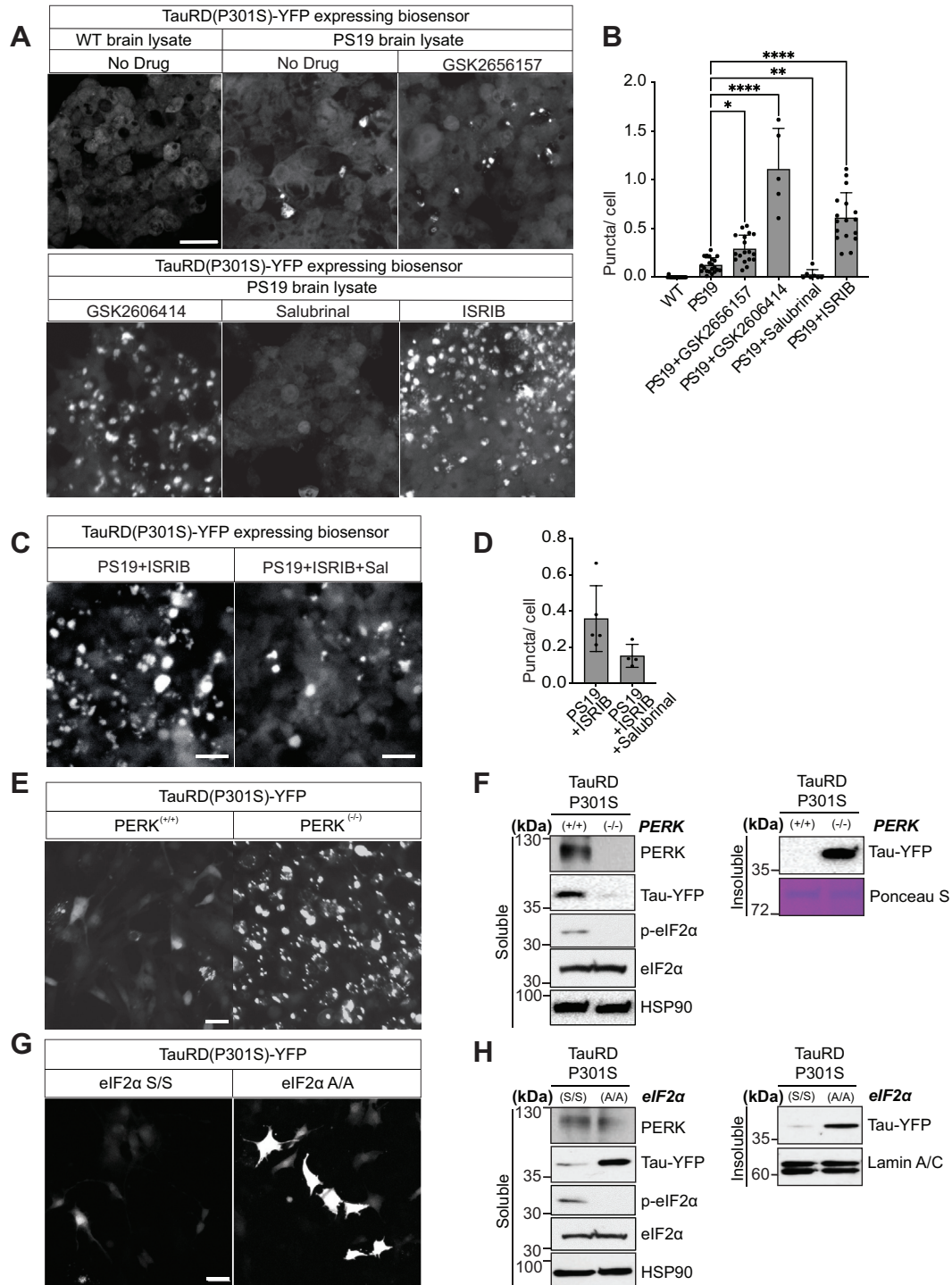
Figure 4. PERK signaling prevents Tau-YFP aggregation. *A*, Biosensor cells were transfected with wildtype or PS19 brain lysate and coincubated with GSK2656157 (5 μM), GSK2606414 (5 μM), Salubrinal (2.5 μM), or ISRIB (5 μM). After 24 h, Tau-YFP fluorescent puncta were imaged by fluorescent microscopy. The scale bar represents 30 μm. *B*, quantification of puncta number from (*A*) normalized by cell number. *P* value was calculated by two-way ANOVA Tukey's multiple comparisons test, mean ± SD. *$p \leq 0.05$, **$p \leq 0.01$, and ****$p \leq 0.0001$ (n ≥ 5 experimental replicates). *C*, Biosensor cells were transfected with PS19 brain lysate and coincubated with ISRIB for 24 h. Media were replaced with/without Salubrinal for another 24 h. Tau-YFP fluorescent puncta were imaged by microscopy after these drug treatments. The scale bar represents 25 μm. *D*, quantification of puncta number from (*C*) normalized by cell number. *E* and *F*, *PERK*^{−/−} or *PERK*^{+/+} MEFs were transduced with TauRD(P301S)-YFP. After 48 h, cells were imaged by fluorescence microscopy (*E*, the scale bar represents 25 μm), and protein lysates were prepared. *F*, soluble protein fractions were immunoblotted for Tau-YFP and HSP90 (loading control). Insoluble fractions were immunoblotted for Tau-YFP and Ponceau stained (loading control). *G* and *H*, *eIF2α*[A/A] or *eIF2α*[S/S] MEFs were transduced with TauRD(P301S)-YFP. After 48 h, cells were imaged by fluorescence microscopy (*G*, the scale bar represents 25 μm), and protein lysates were prepared. *H*, soluble protein fractions were immunoblotted for Tau-YFP or HSP90 (loading control). Insoluble fractions were immunoblotted for Tau-YFP and lamin A/C (loading control). eIF2α, eukaryotic initiation factor 2 alpha; MEF, mouse embryonic fibroblast; PERK, protein kinase R-like endoplasmic reticulum kinase.

PERK dysfunction associated with tauopathy

Last, we tested how chemical modulation of other UPR pathways influenced tau aggregation. When we treated PS19-transfected Biosensor cells with IRE1 inhibitor, 4u8c (47), or ATF6 inhibitor, Ceapin-A7 (48), we saw significant increase in fluorescent tau puncta compared with controls (Fig. 5, *A* and *B*). By contrast, addition of an ATF6 pathway activator, AA147 (49) did not significantly alter the number of fluorescent tau puncta in PS19 brain lysate–transfected cells (Fig. 5, *A* and *B*). Together, these findings support that inhibition of IRE1 and ATF6, like inhibition of PERK signaling, also increases tau aggregation *in vitro*.

PERK signaling is reduced in AD patient hippocampi

Our *in vitro* studies support that reduced PERK signaling leads to increased tau aggregation. To investigate if this relationship between PERK activity and tau aggregation was found *in vivo*, we biochemically analyzed PERK signaling status in frozen hippocampi banked from postmortem brain donors with Braak-staged tau neuropathology (50, 51). We obtained five hippocampi samples from patients with clinical history of AD and Braak VI tau neuropathology (Table 1) and compared with five Braak I control hippocampi (patients with no dementia and no tau neuropathology) (Table 1) We prepared soluble and insoluble protein fractions (52) and confirmed increased pathologic tau protein in Braak VI compared with

Braak I samples (Fig. 6, *A* and *B*). We further confirmed that Braak VI, but not Braak I, brain lysates induced fluorescent puncta formation (tau aggregation) in Biosensor cells (Fig. 6C) consistent with prior studies (32–34, 53, 54). Next, we examined PERK protein expression in these Braak I and VI samples. In the soluble fractions, we found statistically significant reduction of phospho-PERK levels in Braak VI compared with Braak I samples, whereas total PERK levels did not differ (Fig. 6, *D*, *E*, and *F*). PERK phosphorylation is a marker of PERK activation (18), and this finding in Braak I and Braak VI brains provides *in vivo* evidence that reduced PERK pathway activity correlates with increased tau aggregation.

To further investigate if PERK signaling was reduced in AD patient brains, we analyzed mRNA levels of the PERK-regulated gene set in RNA-Seq datasets collected from AD hippocampi and normal hippocampi (Fig. 6, *G–J*). We were not able to perform RNA-Seq on the same brain cases used for immunoblotting because the protein preparation methods were not compatible with the preservation of high-quality RNA. Instead, we examined hippocampal RNA-Seq datasets independently generated from two AD patient cohorts in Japan and the United States (55, 56). The first RNA-Seq dataset contained eight clinically and neuropathologically Braak-staged Alzheimer's brain hippocampi matched with eight control hippocampi collected from Japanese patients
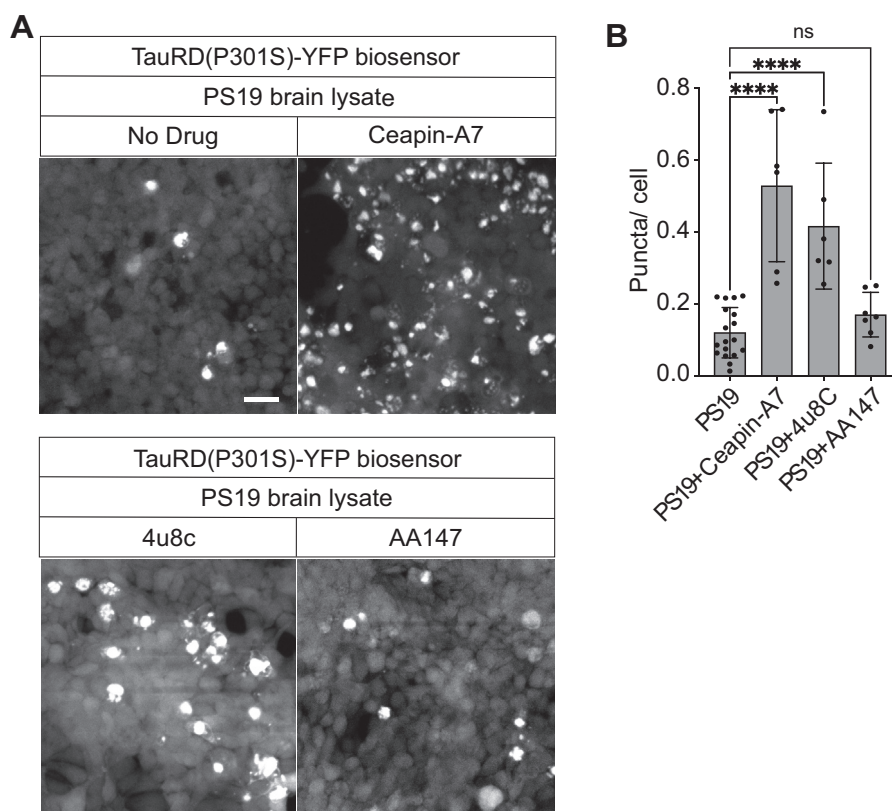
Figure 5. IRE1 and ATF6 pathway inhibitors cause Tau-YFP aggregation in cell culture. Biosensor cells were transfected with PS19 brain lysate and coincubated with ATF6 inhibitor Ceapin-A7 (10 μM), IRE1 inhibitor, 4u8c (10 μM), or ATF6 pathway activator, AA147 (10 μM). After 24 h, Tau-YFP fluorescent puncta were imaged by fluorescent microscopy. The scale bar represents 30 μm. *B*, quantification of puncta number from (*A*) was normalized by cell number. *p* Value was calculated by two-way ANOVA Tukey's multiple comparisons test, mean ± SD, not significant (ns), ****$p \leq 0.0001$ (n ≥ 5 experimental replicates). ATF6, activating transcription factor 6; IRE1, inositol-requiring enzyme 1.

Table 1

Clinicopathologic brain tissue information (age, gender, and Braak staging) of UCSD-ADRC (ADRC brains; brains in Ref. (56) [GSE#173955]; and brains in Ref. (55) [GSE#159699])

UCSD-ADRC brains							
Non-AD brain				**AD brain**			
Sample ID	Braak stage	Sex	Age	Sample ID	Braak stage	Sex	Age
5515	1	F	73	5543	6	M	92
5327	1	M	94	5581	6	F	64
5459	1	M	68	5559	6	F	86
5510	1	M	92	5555	6	M	56
5422	1	M	90	5566	6	F	84
Brains (GSE#173955) (56)							
19	3	F	87	3	5	F	88
20	1	F	80	4	6	F	95
23	Non-AD	M	77	7	6	F	95
24	1	M	55	13	6	F	100
25	1	F	72	14	5	M	99
28	1	F	78	15	6	M	83
30	2	M	80	16	5	M	90
37	Non-AD	M	74	New sample	4	F	84
Brains (GSE#159699) (55)							
10	1/2	M	73	20	5/6	M	64
11	0	M	63	21	5/6	M	63
12	0	M	62	22	5/6	M	71
13	1/2	M	68	23	5/6	M	74
14	1/2	M	70	24	5/6	M	78
15	1/2	M	77	25	5/6	M	61
16	0	M	61	26	5/6	M	65
17	0	M	68	27	5/6	F	70
18	0	M	72	28	5/6	M	79
19	1/2	F	68	29	5/6	M	64
				30	5/6	M	64
				31	5/6	M	67

Abbreviations: F, female; M, male.

((56) and Table 1). The second RNA-Seq dataset contained 12 clinically and neuropathologically Braak-staged Alzheimer's brain hippocampi and 10 normal control hippocampi collected from an American cohort ((55) and Table 1). When we examined the expression levels of the PERK-regulated gene set in these two hippocampal RNA-Seq datasets, we found significantly reduced levels of the PERK-regulated gene set as well as individual PERK-regulated genes in AD brains compared with controls in both Japanese (Fig. 6, *G* and *H*, Suppl. Data 5) and American cohorts (Fig. 6, *I* and *J* and Data S5). Together, our biochemical studies and analyses of published RNA-Seq datasets from Alzheimer's hippocampi provide *in vivo* support that PERK pathway activity inversely correlates with tau pathology.

Discussion

PERK is a key effector of the UPR and ISR and controls translational and transcriptional programs that impact vital cellular processes, including amino acid metabolism, antioxidative response, ER protein folding, autophagy, and apoptosis. In people, ultrarare *PERK* variants that ablate PERK function are causally linked to the autosomal recessive disease WRS. Another distinct group of more common and nonoverlapping *PERK* variants increases risk for tauopathies. Previously, we found that tauopathy-associated *PERK* variants diminished PERK signaling *in vitro* (28), but the consequences of changes in PERK pathway activity on tauopathy pathogenesis remained unclear. Here, we found that impaired PERK

pathway activity increased tau aggregation, whereas increasing p-eIF2α reduced tau aggregation in tauopathy cell culture models. We found that impaired PERK pathway activity correlated with increased tau neuropathology in brain tissues from three different tauopathy patient cohorts. We found that tauopathy-associated PERK variants did not target kinase activity, but instead, at least two variants negatively impacted the tertiary structure of the ER stress–sensing luminal domain. Based on these findings, we propose that tauopathy-associated PERK variants increase disease risk, in part, by facilitating tau protein aggregation and downstream neuropathology.

Our findings showing causality between PERK signaling and tau aggregation were based on experiments performed in MEFs ablated for PERK or eIF2α phosphorylation or in HEK293 cells expressing fluorescent protein–tagged TauRD(P301S). These are robust and reproducible systems to study tau protein aggregation (32–34, 53, 54), but the small TauRD(P301S) fragment likely does not recapitulate all aspects of aggregation by native full-length tau protein isomers. A related limitation of our study is that the MEF and HEK293 cell models do not recapitulate the neuronal and glial environments where tau causes neuropathology. It will be important to evaluate how tauopathy-associated PERK variants impact tau pathology in native neural cell types. Despite the limitations of our abbreviated tau construct and cell culture models, our analyses of PERK signaling in primary patient brain tissues support that reduced PERK pathway activity correlates with increased tau protein aggregation and pathology. Given the absence of therapies for tauopathies and the
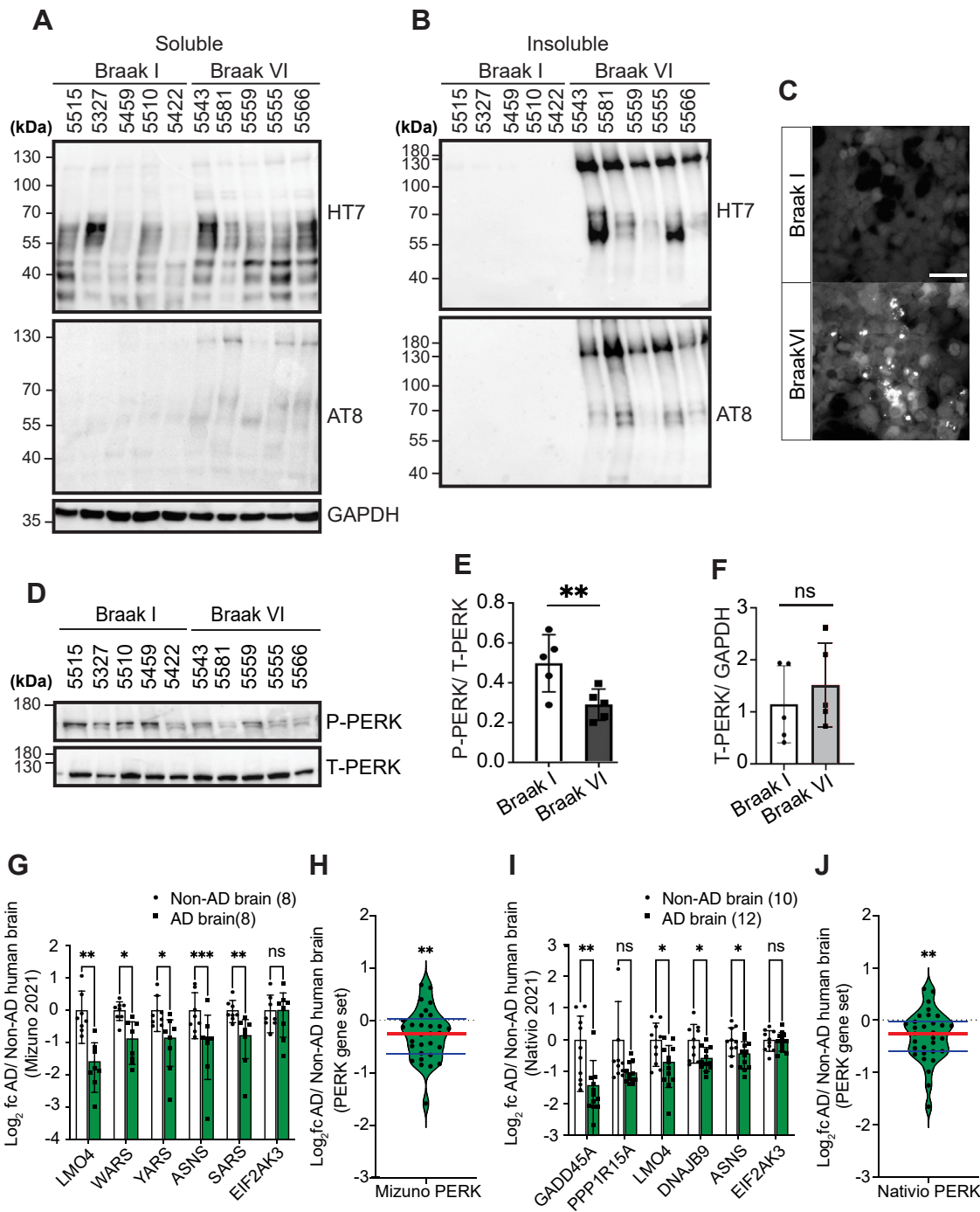
Figure 6. PERK pathway activity is reduced in Alzheimer's disease (AD) patient brains. *A* and *B*, protein lysates were prepared from 1 mg of five Braak I (normal) and five Braak VI (AD) patient hippocampi. Soluble (*A*) and insoluble (*B*) protein lysate fractions were immunoblotted for total human Tau (HT7), phospho-Tau (AT8), and GAPDH (loading control). Individual brain identification numbers are listed above the blots, and associated clinicopathology information are provided in Table 1. *C*, Biosensor cells were transfected with normal (Braak I) or AD (Braak VI) soluble brain lysate. After 24 h, Tau-YFP aggregates (fluorescent puncta) were imaged by fluorescent microscopy. The scale bar represents 50 μm. *D–F*, soluble brain lysates from (*A*) were immunoblotted for phospho-PERK and total PERK; protein levels were quantified by densitometry and normalized by loading controls, PERK (*D*) and GAPDH (*A*). PERK was not detected in insoluble fraction (Fig. S3). **$p \leq 0.01$, not significant (ns), two-tailed Student's *t* test. Mean ± SD. *G* and *H*, gene expression levels of PERK-regulated genes in hippocampi of AD brains (n = 8) relative to non-AD brains (n = 10) from GSE173955 (56) are shown as $\log_2$ fold change. The graph (*G*) shows levels of the five PERK-regulated genes most significantly reduced between AD brains and non-AD brains and expression levels of *PERK* gene itself. The violin plot (*H*) shows levels of the entire PERK-regulated gene set. Detailed clinicopathology information are available from Ref. (56) and summarized in Table 1. *I* and *J*, gene expression levels of PERK-regulated genes from hippocampi of AD brains (n = 12) relative to non-AD brains (n = 10) from Ref. (55) (GSE159699) are shown as $\log_2$ fold change. The graph (*I*) shows levels of the five PERK-regulated genes most significantly reduced between AD and non-AD brains and *PERK* gene expression levels itself. The violin plot (*J*) shows levels of the entire PERK-regulated gene set. Detailed clinicopathology information of these AD and non-AD brains are available from Ref. (55) and summarized in Table 1. Error bars in *G* and *I* represent mean ± SD. *Black circles* and *squares* represent individual AD or non-AD brains. (*$p \leq 0.05$, **$p \leq 0.01$, ***$p \leq 0.001$, not significant [ns], two-tailed Student's *t* test). The *red horizontal line* in figures *H* and *J* marks the median level of gene expression, and the *thin horizontal blue lines* delimit upper and lower gene expression quartiles in the violin plots. (**$p \leq 0.01$, one-sample *t* test and two-tailed Wilcoxon signed rank test). PERK, protein kinase R-like endoplasmic reticulum kinase.

potential of small-molecule PERK and ISR pathway agents to influence tau aggregation, the role of PERK signaling warrants further investigation in the pathogenesis and treatment of tauopathies.

An unexpected finding in our analysis of human *PERK* variants was the unequal distribution of the tauopathy-risk *haplotype B* allele between racial/ethnic groups ranging from a low of ∼5% in African populations up to 49% in East Asian populations (Fig. 1*C*). Prior studies found increased prevalence of PSP in a Japanese cohort (17.90 per 100,000 people) (57), compared with 6 per 100,000 in a European cohort (58, 59); and 2.95 per 100,000 in the US population. We speculate that the increased prevalence of PSP in the Japanese populace could reflect the higher prevalence of the tauopathy disease allele, *haplotype B*, in this East Asian population. PSP prevalence has not been examined in African groups, but we predict that PSP prevalence should be significantly lower because of the relative rarity of the *haplotype B* in this population (Fig. 1*C*). Additional molecular epidemiologic studies across different ethnic/racial groups can shed light upon the link between *haplotype B* prevalence and distribution of disease.

We observed that many tauopathy-associated PERK variants target the ER stress–sensing luminal domain (Fig. 1*E*), and modeling of amino acid substitutions at residues 136 and 240 on the mammalian crystal structure of the PERK luminal domain revealed disruption of H-bonds between these two residues when converted to disease variants (Fig. 2). How do these changes in the luminal domain impact PERK signaling? The local sequences bearing residues 136 and 240 are important for PERK tetramerization/oligomerization in response to ER stress (30, 31), and therefore, we speculate that the S136C and R240H conversions may alter the tetramerization/oligomerization ability of PERK. The luminal domain of PERK also binds to chaperones, and luminal domain PERK variants may also alter interactions with PERK regulatory cofactors like Grp78/BiP (30, 60). PERK dimerization after ER stress is less likely to be directly affected by changes at S136 and R240 because these residues are not located near the PERK dimerization interface (30). Based on these modeling observations, we propose that tauopathy variants in the PERK luminal domain interfere with the ability of PERK to accurately sense and respond to ER stress; dysregulation of kinase activation and downstream signaling arises as a secondary consequence.

The status of PERK signaling and ER stress in tauopathy pathogenesis is mixed. Biochemical analysis of tauopathy mouse brains at many ages prior to and during disease revealed no increase of PERK signaling or induction of ER stress in these models (61, 62). By contrast, increased PERK signaling was reported in some diseased neurons through immunostaining of primary AD and PSP patient brain sections (63, 64). In our studies, we saw no activation of PERK signaling in the cell culture tau aggregation model or in primary tauopathy patient hippocampi (Figs. 3 and 6). Our PERK signaling analysis was performed by Western blots or RNA-Seq of bulk lysates from *in vitro* cultured cells or human brain tissues. This approach may mask increased PERK signaling in individual or small populations of cells. Single-cell approaches can provide better resolution of PERK signaling dysregulation during tau aggregation in distinct neural cell types.

In our studies, we not only saw no activation of PERK signaling but instead, we saw reduced PERK signaling in the HEK293 cell culture model and in tauopathy patient brain samples by gene expression measurements (Figs. 3 and 6). To our knowledge, reduced PERK signaling in tauopathy has not been reported previously. We do not know how or why PERK signaling as determined by transcriptional output is suppressed in the cell culture model of tau aggregation or in advanced tauopathy patient brains. However, impaired PERK function worsens ER homeostasis, increases oxidative stress, and increases protein misfolding (45). In the brain, increased tau aggregation could be a specific deleterious consequence of PERK dysfunction.

Our findings support prior studies that pharmacologic PERK activation or PERK overexpression attenuate tau pathology *in vitro* and *in vivo* (65). Augmented PERK signaling, and more broadly UPR/ISR signaling, may provide tools to ensure tau protein homeostasis and prevent the emergence of pathologic tau aggregates. A PERK augmentation strategy would be especially applicable for carriers of tauopathy-associated *PERK* hypomorph alleles.

Experimental procedures

Genome data collection and interpretation of PERK variants

About 1294 PERK variants were examined in three publicly available databases (accessed date: January 5, 2022): the Genome Aggregation Database (gnomAD, version 2.1.1), ClinVar (National Center for Biotechnology Information [NCBI]), and European Bioinformatics Institute (EMBL-EBI) Database. The 1294 variants included 479 missense variants, 447 intron variants, 226 silent variants, 51 splicing variants, 37 UTR variants, 19 frameshift variants, 19 start and stop variants, and 16 in-frame variants. 12 WRS and 18 tauopathy missense mutations were identified in the genome databases and in various publications (https://uswest.ensembl.org/Homo_sapiens/Gene/Phenotype?db=core;g=ENSG00000172071;r=2:88556741-88627464; https://www.ncbi.nlm.nih.gov/CBBresearch/Lu/Demo/LitVar/index.html#!?query=EIF2AK3; https://gnomad.broadinstitute.org/gene/ENSG00000172071?dataset=gnomad_r2_1) (Fig. 1). PERK haplotype race/ethnic frequency was calculated by population allele count divided by allele number from the gnomAD database. Tauopathy-related mutations were grouped as common ≥1%, 0.1% ≤ rare <1%, and ultrarare <0.1% based on the population allele frequencies identified from gnomAD. Pathogenicity of PERK variants was assessed by publicly accessible Web server–based prediction tools (PolyPhen-2: http://genetics.bwh.harvard.edu/pph2/; PROVEAN: http://provean.jcvi.org/index.php; MutationTaster: https://www.mutationtaster.org/; SIFT: https://sift.bii.a-star.edu.sg/www/SIFT_seq_submit2.html; and https://cadd.gs.washington.edu/. All last accessed June 2021). PolyPhen-2 (Polymorphism Phenotyping v2) uses sequence alignments, phylogenetics, and structural data to characterize amino acid

substitutions and calculates a score for the variant, classifying it as "benign," "possibly damaging," or "probably damaging." Scores range from 0.0 (benign) to 1.0 (probably damaging). SIFT predicts the impact of an amino acid change on protein function by comparing amino acid alignments from related sequences to calculate a "SIFT score": 0 to 0.05 will be classified as "damaging," 0.05 to 1 as "tolerated." Prediction of pathological mutations on proteins uses sequence information for its neural network and predicts the effect of amino acid changes on protein function, by calculating a reliability index ranging from 0 to 10 (most unreliable to most reliable prediction) and a prediction of either "neutral" or "pathological." Mutation prediction is based on SIFT and structural and functional properties of proteins. Mutation prediction was created using disease-associated mutations from HGMD and neutral amino acid substitutions from Swiss-Prot. The output contains a general score, (g) where $g > 0.5$ ($p < 0.05$) is actionable, $g > 0.75$ ($p < 0.05$) is confident, and $g > 0.75$ ($p < 0.01$) is very confident that an amino acid substitution is likely to have a phenotypic effect. All data collection, pathogenicity assessments, and database annotation were performed by scientists trained with standardized training modules and annual proficiency testing.

PERK luminal domain structural modeling analysis

Protein sequence alignment was evaluated using the EMBL-EBI EMBOSS Needle program (https://www.ebi.ac.uk/Tools/psa/emboss_needle/) and visualized using JalView (version 2.11.1.4; www.jalview.org). The visualization of the reconstructed model structure and H-bond prediction of the PERK protein was prepared using PyMol molecular graphics system (http://www.pymol.org). The crystal structure of mammalian PERK luminal domain (PDB ID: 4YZY) was used for the structure modeling analysis. When superimposed 4YZY with the mutation models, all H-bonds of residues R240/H240 and S136/C136 were highlighted and shown in *dashed lines*.

Antibodies and chemicals

Antibodies including HT-7 (catalog no.: MN1000; Invitrogen), AT8 (catalog no.: MN1020; Invitrogen), YFP (catalog no.: ab6556; Abcam), HSP90 (catalog no.: ab13492; Abcam), lamin A/C (catalog no.: 2032; Cell Signaling Technology), GAPDH (catalog no.: ab8245; Abcam), T-PERK (catalog no.: 3192; Cell Signaling Technology), phosphorylated PERK (catalog no.: 3179; Cell Signaling Technology), eIF2α (catalog no.: 5324; Cell Signaling Technology), p-eIF2α (catalog no.: 5324; Cell Signaling Technology) were pretested to detect the targeted proteins. Small molecules included GSK2656157 (catalog no.: 9466-5; BioVision), GSK2606414 (catalog no.: S7307; Selleckchem), salubrinal (catalog no.: S2923; Selleckchem), ISRIB (catalog no.: S7400; Selleckchem); Ceapin-A7 (catalog no.: SML2330; Sigma−Aldrich), 4u8C (catalog no.: CAS14003-96-4; Calbiochem), and AA147 (product no.: 6538059; ChemBridge) were prepared in dimethyl sulfoxide following the manufacturer's instruction and stored at −80 °C as stock solution. ER stress−inducing chemical, thapsigargin, was dissolved in dimethyl sulfoxide and added to the cell culture media at a concentration of 300 nM. The working solutions were freshly prepared with −80 °C stock solution.

Mouse and human brain protein lysate preparation

Mouse brain extraction

P301S tau transgenic (PS19) mice (B6; C3-Tg(Prnp-MAPT*P301S)PS19Vle/J; stock number: 008169; Jackson Laboratory) harboring T34 isoform of *MAPT* with one N-terminal insert and four microtubule-binding repeats (1N4R) encoding the human P301S mutation were obtained from Jackson Laboratory and maintained in a C57Bl/6j genetic background in standard vivarium environment (12 h light:12 h dark cycle). Approved laboratory personnel checked mice during the light phase of the light:dark cycle to determine birthdates and weaned the new pups in 3 weeks. At 6 months, PS19 and WT male littermates were anesthetized with ketamine/xylazine (1 mg/kg) followed by intracardiac perfusion with saline. Then, mice were euthanized by carbon dioxide and cervical dislocation, and brains were subsequently removed following institutional guidelines and with Institutional Animal Care and Use Committee approval. Fresh brains were then homogenized with Dounce homogenizer in ice-cold 1× radioimmunoprecipitation assay (RIPA) buffer with protease inhibitor (catalog no.: S8820; Sigma−Aldrich). Following centrifugation (13,000 rpm) at 4 °C for 20 min, the soluble fraction was analyzed for protein concentration and frozen. The supernatants were aliquoted and stored at −80°C until further use. The insoluble fraction was vigorously resuspended by vortex and boiled with 4× SDS sample buffer for 10 min. About 10 μg of total protein was run on an 1 to 15% Bis−Tris gel and transferred to nitrocellulose for Western blotting.

Human brain extraction

Frozen human brain tissues were obtained from UC San Diego Alzheimer Disease Research Center (UCSD-ADRC). The diagnoses and demographics in Table 1 were obtained from patients neurologically and psychometrically studied at the UCSD-ADRC with institutional institutional review board approval. Patients gave informed consent for postmortem brain sample collection for research purposes. Upon autopsy, patient brains were collected by the UCSD-ADRC Neuropathology Core and sagittally divided; the left hemibrain was fixed in 10% buffered formalin for neuropathological analysis for Braak tau staging; and the right hemibrain sections were frozen at −70 °C for subsequent protein isolation. For this study, frozen hippocampal tissues were obtained. Human brain protein lysate extraction followed the previous literature (52). In brief, 0.3 g of brain tissue was homogenized on ice with 5.3× volume (w/v) Goedert buffer composed of 10 mM Tris−HCl, pH = 7.4, 0.8 M NaCl, 1 mM EGTA, and 10% sucrose including protease inhibitor, *cOmplete* mini (catalog no.: 11836153001; Roche), per 10 ml and the remaining solution volume with pure PMSF. The homogenate mixture was then spun at 20,000*g* for 20 min. The supernatants were retained afterward and rehomogenized in 2.65× volume (w/v) of

Goedert buffer. The homogenates were spun at 20,000g for 20 min. The previous supernatant was then combined with newly retained supernatant, and 20 μl supernatant was saved for protein concentration. Afterward, 1% of *N*-lauroylsarcosine (catalog no.: L7414; Sigma–Aldrich) was added to the combined supernatant and rocked the mixture for 1 h at room temperature. After 1 h, the mixture was spun for another hour at 100,000g. The supernatant was saved as a soluble extract. The dark red brown pellet was then resuspended in 50 mM Tris–HCl, pH = 7.5, at 0.2 ml of mixture per gram of pellet, then stored at 4 °C for further biochemical experiments.

Biosensor analysis

Cell culture

"Biosensor" HEK293 cells stably expressing TauRD(P301S)-YFP were generated as previously described (32, 34). Biosensor cells were maintained in a humidified 37 °C, 5% CO$_2$ incubator in Dulbecco's modified Eagle's medium (Gibco) and supplemented with 10% fetal bovine serum with 1% penicillin/streptomycin (Gibco).

Brain lysate transfection

Tau brain lysate transfection was performed as previously described (32, 34). In brief, Biosensor cells were plated at a density of 0.5×10^3 cells per well in a 12-well plate (catalog no.: 07-200-82; Corning). Twenty-four hours later, at ∼20∼25% confluency, cells were transduced with PS19 or control brain lysate. Transduction complexes were composed of 50 μl Opti-MEM (catalog no.: 31985070; Thermo Fisher), 3 μl LT-1 transfection reagent (catalog no.: MIR2020; Mirus Bio LLC), and 1 μl brain lysate (1 μg/μl stock determined by bicinchoninic acid [catalog no.: 5000001; Bio-Rad Protein Assay Kit I]). After 24 h, cells were fixed with 4% paraformaldehyde/3% sucrose fixation solution in PBS and imaged using ZEISS 710 confocal microscope.

Pharmacochemical modulation of tau aggregation

After 24 h, culture media were replaced with fresh media with either PERK pathway inhibitors (GSK2656157, GSK2606414, or ISRIB) or modulators (salubrinal or Selphin-1) for another 24 h or more. Live cell imaging was performed using ZEISS 710 confocal microscope at 37 °C, 5% CO$_2$.

Tau aggregation in MEFs

$PERK^{+/+}$ or $PERK^{-/-}$, and $eIF2\alpha^{S/S}$ or $eIF2\alpha^{A/A}$ MEF cells were transiently transduced with TauRD(P301S)-YFP plasmid using *TransIT* LT-1 Transfection reagent (catalog no.: MIR2020; Mirus Bio LLC) and virally transduced by lab-prepared lentiviral infection following the manufacturer's instruction and incubated for 2 days. The cells were lysed with RIPA buffer, centrifuged at 14,000g for 10 min at 4 °C; the supernatants were saved for the Western blot analysis. Cell imaging analysis was performed using ZEISS 710 confocal microscope.

Preparation of lentivirus

Lentivirus expressing TauRD(P301S)-YFP was prepared following Addgene lentivirus culture protocol. In brief, 293T packaging cells at 3×10^6 cells per plate in DMEM complete media was plated in 10 cm cell culture dish. The TauRD(P301S)-YFP plasmid DNA with virus packing pDNAs (psPAX2; pMD2.G; Addgene) was transfected into 293T cells by 1 mg/ml polyethyleneimine transfection reagent and incubated for 36 h. The resultant media were centrifuged at 150,000g for 90 min at 4 °C. The concentrated virus was collected and stored at −80 °C until further infection.

Immunoblotting analysis

$PERK^{+/+}$ and $PERK^{-/-}$; $eIF2\alpha^{S/S}$ and $eIF2\alpha^{A/A}$ MEFs transduced with TauRD-YFP and Biosensor cell transfected with wildtype and PS19 brain lysates were lysed with SDS lysis buffer (2% SDS in PBS containing protease and phosphatase inhibitors [catalog no.: 11836153001; Roche]) or RIPA buffer. Protein concentrations of the cell lysates were determined by bicinchoninic acid protein assay (Pierce). Equal amounts of protein were loaded onto 4 to 15% Mini-PROTEAN TGX precasted gels (Bio-Rad) and immunoblotted. The following antibodies and dilutions were used: anti-HT-7 at 1:1000 dilution, AT8 at 1:1000 dilution, YFP at 1:1000 dilution, HSP90 at 1:2000 dilution, lamin A/C at 1:3000 dilution, GAPDH at 1:3000 dilution, T-PERK at 1:1000 dilution, phosphorylated PERK at 1:1000 dilution, eIF2α at 1:1000 dilution, and p-eIF2α at 1:1000 dilution. After overnight incubation with primary antibody, membranes were washed in Tris-buffered saline with 0.1% Tween-20, followed by incubation of a horseradish peroxidase–coupled secondary antibody (Cell Signaling). Immunoreactivity was detected using the SuperSignal West chemiluminescent substrate (Pierce) and BIO-RAD Universal Gel Molecular Imager.

RNA-Seq analysis

RNA-Seq analysis was performed as previously described (36). In brief, frozen cells were collected, and RNA extraction, RNA quality control, and RNA-Seq were performed by BGI DNBSEQ Eukaryotic Strand-specific Transcriptome Resequencing (BGI); DNBSEQ stranded mRNA library, providing paired-end 100 bp reads at 30 million reads per sample. The sequencing data were filtered with SOAPnuke (version 1.5.2) (66) and clean reads were mapped using HISAT2 (version 2.0.4) to the reference genome (Homo_sapiens_GCF_000001405.38_GRCh38.p12 reference assembly) (67, 68). The expression levels of the genes were calculated by RSEM (version 1.2.12) (69). Differential expression analysis and statistical significance calculations between condition and experiment groups were assessed using R-based software, DESeq2 (version: 1.4.5) (70). The false discovery rate q value for the DESeq analysis is 0.1 (70). ER stress gene sets were collected from the results of the DESeq2 analysis and visualized using GraphPad Prism (GraphPad Software, Inc) software. Violin plots comparing PS19 brain lysate transfection group and wildtype brain lysate transfection group were generated

with the Log2 fold change data of the differential expression analysis.

Human AD brain RNA-Seq analysis

Human AD brain RNA-Seq datasets were collected from the NCBI Gene Expression Omnibus database: GSE173955 (56) and GSE159699 (55). Individual ER stress gene set of AD brains was extracted and normalized by non-AD control brain in each dataset and visualized using GraphPad Prism software. Violin plots comparing non-AD brain group and AD brain group were generated with the Log2 fold change data of the differential expression analysis.

GSEA and GO analysis

gProfiler, a web-based application (https://biit.cs.ut.ee/gprofiler/), was used for GO pathway enrichment analysis. The gene sets from the bulk RNA-Seq analysis (Biosensor cell and human AD brain analysis: GSE173955 (56) and GSE159699 (55)) were entered, and GO terms based on significant association were collected ($p < 0.05$). GSEA software was downloaded (https://www.broadinstitute.org/gsea/) and also used to analyze the gene sets. Preranked lists were entered with the same gene sets and ranked based on expression values relative to wildtype controls. Weighted analysis with the GO reference database was performed, and GSEA enrichment plots were presented.

Statistical analysis

For RNA-Seq gene expression data, differential gene expression analysis (DESeq) and the statistical significance (p value) of differences between control and experimental groups (n = 5 independent replicates) were assessed using R-based software, DESeq2 (version: 1.4.5) (70). The false discovery rate q value for the DESeq analysis is 0.1 (70); For the IRE1-, PERK-, ATF6-, and ERAD-regulated gene groups, the one-sample t test and Wilcoxon signed rank test were used to calculate statistical significance of differences in the gene groups between control and experimental conditions. For individual genes, two-tailed Student's t test was used to calculate statistical significance of differences in gene expression between control and experimental conditions. For protein levels, two-tailed Student's t test was used to calculate the statistical significance of differences in protein levels between control and experimental conditions from immunoblot images captured by ImageJ (the National Institutes of Health and the Laboratory for Optical and Computational Instrumentation (LOCI, University of Wisconsin)) and normalized to loading control images. For Biosensor cell aggregate puncta analysis, we used ImageJ to count cells and puncta visualized by confocal fluorescence microscopy and performed Student's t test and ANOVA test followed by Tukey's multiple comparisons test. The results were used with averages of all experiments ± SD. A probability of less than 0.05 was considered statistically significant and was annotated as $*p \leq 0.05$, $**p \leq 0.01$, $***p \leq 0.001$, and $****p \leq 0.0001$. All statistics were calculated using GraphPad Prism 9 software.

Data availability

The RNA-Seq raw data and differential gene expression analyses from Biosensor cells are available under Gene Expression Omnibus accession number GSE217525.

References

1. Dickson, D. W., Rademakers, R., and Hutton, M. L. (2007) Progressive supranuclear palsy: pathology and genetics. *Brain Pathol.* **17**, 74–82
2. Kidd, M. (1963) Paired helical filaments in electron microscopy of Alzheimer's disease. *Nature* **197**, 192–193

3. Wischik, C. M., Novak, M., Thogersen, H. C., Edwards, P. C., Runswick, M. J., Jakes, R., *et al.* (1988) Isolation of a fragment of tau derived from the core of the paired helical filament of Alzheimer disease. *Proc. Natl. Acad. Sci. U. S. A.* **85**, 4506–4510

4. Lee, V. M., Goedert, M., and Trojanowski, J. Q. (2001) Neurodegenerative tauopathies. *Annu. Rev. Neurosci.* **24**, 1121–1159

5. Wang, Y., and Mandelkow, E. (2016) Tau in physiology and pathology. *Nat. Rev. Neurosci.* **17**, 5–21

6. Lee, G., Cowan, N., and Kirschner, M. (1988) The primary structure and heterogeneity of tau protein from mouse brain. *Science* **239**, 285–288

7. Goedert, M., Wischik, C. M., Crowther, R. A., Walker, J. E., and Klug, A. (1988) Cloning and sequencing of the cDNA encoding a core protein of the paired helical filament of Alzheimer disease: Identification as the microtubule-associated protein tau. *Proc. Natl. Acad. Sci. U. S. A.* **85**, 4051–4055

8. Drubin, D. G., Caput, D., and Kirschner, M. W. (1984) Studies on the expression of the microtubule-associated protein, tau, during mouse brain development, with newly isolated complementary DNA probes. *J. Cell Biol.* **98**, 1090–1097

9. Goedert, M., and Jakes, R. (1990) Expression of separate isoforms of human tau protein: correlation with the tau pattern in brain and effects on tubulin polymerization. *EMBO J.* **9**, 4225–4230

10. Adams, S. J., DeTure, M. A., McBride, M., Dickson, D. W., and Petrucelli, L. (2010) Three repeat isoforms of tau inhibit assembly of four repeat tau filaments. *PLoS One* **5**, e10810

11. Schmitt, F. O. (1968) Fibrous proteins–neuronal organelles. *Proc. Natl. Acad. Sci. U. S. A.* **60**, 1092–1101

12. Barghorn, S., and Mandelkow, E. (2002) Toward a unified scheme for the aggregation of tau into Alzheimer paired helical filaments. *Biochemistry* **41**, 14885–14896

13. Hoglinger, G. U., Melhem, N. M., Dickson, D. W., Sleiman, P. M., Wang, L. S., Klei, L., *et al.* (2011) Identification of common variants influencing risk of the tauopathy progressive supranuclear palsy. *Nat. Genet.* **43**, 699–705

14. Ferrari, R., Ryten, M., Simone, R., Trabzuni, D., Nicolaou, N., Hondhamuni, G., *et al.* (2014) Assessment of common variability and expression quantitative trait loci for genome-wide associations for progressive supranuclear palsy. *Neurobiol. Aging* **35**, 1514 e1511–1512

15. Sanchez-Contreras, M. Y., Kouri, N., Cook, C. N., Serie, D. J., Heckman, M. G., Finch, N. A., *et al.* (2018) Replication of progressive supranuclear palsy genome-wide association study identifies SLCO1A2 and DUSP10 as new susceptibility loci. *Mol. Neurodegener.* **13**, 37

16. Liu, Q. Y., Yu, J. T., Miao, D., Ma, X. Y., Wang, H. F., Wang, W., *et al.* (2013) An exploratory study on STX6, MOBP, MAPT, and EIF2AK3 and late-onset Alzheimer's disease. *Neurobiol. Aging* **34**, 1519 e1513–1517

17. Wong, T. H., van der Lee, S. J., van Rooij, J. G. J., Meeter, L. H. H., Frick, P., Melhem, S., *et al.* (2019) EIF2AK3 variants in Dutch patients with Alzheimer's disease. *Neurobiol. Aging* **73**, 229.e211–229.e218

18. Harding, H. P., Zhang, Y., and Ron, D. (1999) Protein translation and folding are coupled by an endoplasmic-reticulum-resident kinase. *Nature* **397**, 271–274

19. Ron, D., and Harding, H. P. (2012) Protein-folding homeostasis in the endoplasmic reticulum and nutritional regulation. *Cold Spring Harb. Perspect. Biol.* **4**, a013177

20. Walter, P., and Ron, D. (2011) The unfolded protein response: from stress pathway to homeostatic regulation. *Science* **334**, 1081–1086

21. Harding, H. P., Novoa, I., Zhang, Y., Zeng, H., Wek, R., Schapira, M., *et al.* (2000) Regulated translation initiation controls stress-induced gene expression in mammalian cells. *Mol. Cell* **6**, 1099–1108

22. Harding, H. P., Zhang, Y., Zeng, H., Novoa, I., Lu, P. D., Calfon, M., *et al.* (2003) An integrated stress response regulates amino acid metabolism and resistance to oxidative stress. *Mol. Cell* **11**, 619–633

23. Han, J., Back, S. H., Hur, J., Lin, Y. H., Gildersleeve, R., Shan, J., *et al.* (2013) ER-stress-induced transcriptional regulation increases protein synthesis leading to cell death. *Nat. Cell Biol.* **15**, 481–490

24. Novoa, I., Zeng, H., Harding, H. P., and Ron, D. (2001) Feedback inhibition of the unfolded protein response by GADD34-mediated dephosphorylation of eIF2alpha. *J. Cell Biol.* **153**, 1011–1022

25. Harding, H. P., Zeng, H., Zhang, Y., Jungries, R., Chung, P., Plesken, H., *et al.* (2001) Diabetes mellitus and exocrine pancreatic dysfunction in perk-/- mice reveals a role for translational control in secretory cell survival. *Mol. Cell* **7**, 1153–1163

26. Delepine, M., Nicolino, M., Barrett, T., Golamaully, M., Lathrop, G. M., and Julier, C. (2000) EIF2AK3, encoding translation initiation factor 2-alpha kinase 3, is mutated in patients with Wolcott-Rallison syndrome. *Nat. Genet.* **25**, 406–409

27. Julier, C., and Nicolino, M. (2010) Wolcott-Rallison syndrome. *Orphanet J. Rare Dis.* **5**, 29

28. Yuan, S. H., Hiramatsu, N., Liu, Q., Sun, X. V., Lenh, D., Chan, P., *et al.* (2018) Tauopathy-associated PERK alleles are functional hypomorphs that increase neuronal vulnerability to ER stress. *Hum. Mol. Genet.* **27**, 3951–3963

29. Liu, J., Hoppman, N., O'Connell, J. R., Wang, H., Streeten, E. A., McLenithan, J. C., *et al.* (2012) A functional haplotype in EIF2AK3, an ER stress sensor, is associated with lower bone mineral density. *J. Bone Miner Res.* **27**, 331–341

30. Carrara, M., Prischi, F., Nowak, P. R., and Ali, M. M. (2015) Crystal structures reveal transient PERK luminal domain tetramerization in endoplasmic reticulum stress signaling. *EMBO J.* **34**, 1589–1600

31. Wang, P., Li, J., and Sha, B. (2016) The ER stress sensor PERK luminal domain functions as a molecular chaperone to interact with misfolded proteins. *Acta Crystallogr. D Struct. Biol.* **72**, 1290–1297

32. Holmes, B. B., Furman, J. L., Mahan, T. E., Yamasaki, T. R., Mirbaha, H., Eades, W. C., *et al.* (2014) Proteopathic tau seeding predicts tauopathy *in vivo*. *Proc. Natl. Acad. Sci. U. S. A.* **111**, E4376–4385

33. Woerman, A. L., Stohr, J., Aoyagi, A., Rampersaud, R., Krejciova, Z., Watts, J. C., *et al.* (2015) Propagation of prions causing synucleinopathies in cultured cells. *Proc. Natl. Acad. Sci. U. S. A.* **112**, E4949–4958

34. Kaufman, S. K., Sanders, D. W., Thomas, T. L., Ruchinskas, A. J., Vaquer-Alicea, J., Sharma, A. M., *et al.* (2016) Tau prion Strains dictate patterns of cell pathology, progression rate, and regional vulnerability *in vivo*. *Neuron* **92**, 796–812

35. Yoshiyama, Y., Higuchi, M., Zhang, B., Huang, S. M., Iwata, N., Saido, T. C., *et al.* (2007) Synapse loss and microglial activation precede tangles in a P301S tauopathy mouse model. *Neuron* **53**, 337–351

36. Kroeger, H., Grandjean, J. M. D., Chiang, W. J., Bindels, D. D., Mastey, R., Okalova, J., *et al.* (2021) ATF6 is essential for human cone photoreceptor development. *Proc. Natl. Acad. Sci. U. S. A.* **118**, a013177

37. Lu, P. D., Jousse, C., Marciniak, S. J., Zhang, Y., Novoa, I., Scheuner, D., *et al.* (2004) Cytoprotection by pre-emptive conditional phosphorylation of translation initiation factor 2. *EMBO J.* **23**, 169–179

38. Lee, A. H., Iwakoshi, N. N., and Glimcher, L. H. (2003) XBP-1 regulates a subset of endoplasmic reticulum resident chaperone genes in the unfolded protein response. *Mol. Cell Biol.* **23**, 7448–7459

39. Bommiasamy, H., Back, S. H., Fagone, P., Lee, K., Meshinchi, S., Vink, E., *et al.* (2009) ATF6alpha induces XBP1-independent expansion of the endoplasmic reticulum. *J. Cell Sci.* **122**, 1626–1636

40. Wu, J., Rutkowski, D. T., Dubois, M., Swathirajan, J., Saunders, T., Wang, J., *et al.* (2007) ATF6alpha optimizes long-term endoplasmic reticulum function to protect cells from chronic stress. *Dev. Cell* **13**, 351–364

41. Axten, J. M., Medina, J. R., Feng, Y., Shu, A., Romeril, S. P., Grant, S. W., *et al.* (2012) Discovery of 7-methyl-5-(1-{[3-(trifluoromethyl)phenyl]acetyl}-2,3-dihydro-1H-indol-5-yl)-7H-p yrrolo[2,3-d]pyrimidin-4-amine (GSK2606414), a potent and selective first-in-class inhibitor of protein kinase R (PKR)-like endoplasmic reticulum kinase (PERK). *J. Med. Chem.* **55**, 7193–7207

42. Sidrauski, C., Acosta-Alvear, D., Khoutorsky, A., Vedantham, P., Hearn, B. R., Li, H., *et al.* (2013) Pharmacological brake-release of mRNA translation enhances cognitive memory. *eLife* **2**, e00498

43. Rojas-Rivera, D., Delvaeye, T., Roelandt, R., Nerinckx, W., Augustyns, K., Vandenabeele, P., *et al.* (2017) When PERK inhibitors turn out to be new potent RIPK1 inhibitors: critical issues on the specificity and use of GSK2606414 and GSK2656157. *Cell Death Differ.* **24**, 1100–1110

44. Boyce, M., Bryant, K. F., Jousse, C., Long, K., Harding, H. P., Scheuner, D., *et al.* (2005) A selective inhibitor of eIF2alpha dephosphorylation protects cells from ER stress. *Science* **307**, 935–939

45. Harding, H. P., Zhang, Y., Bertolotti, A., Zeng, H., and Ron, D. (2000) Perk is essential for translational regulation and cell survival during the unfolded protein response. *Mol. Cell* **5**, 897–904

46. Scheuner, D., Song, B., McEwen, E., Liu, C., Laybutt, R., Gillespie, P., *et al.* (2001) Translational control is required for the unfolded protein response and *in vivo* glucose homeostasis. *Mol. Cell* **7**, 1165–1176

47. Cross, B. C., Bond, P. J., Sadowski, P. G., Jha, B. K., Zak, J., Goodman, J. M., *et al.* (2012) The molecular basis for selective inhibition of unconventional mRNA splicing by an IRE1-binding small molecule. *Proc. Natl. Acad. Sci. U. S. A.* **109**, E869–878

48. Gallagher, C. M., Garri, C., Cain, E. L., Ang, K. K., Wilson, C. G., Chen, S., *et al.* (2016) Ceapins are a new class of unfolded protein response inhibitors, selectively targeting the ATF6alpha branch. *eLife* **5**, e11878

49. Plate, L., Cooley, C. B., Chen, J. J., Paxman, R. J., Gallagher, C. M., Madoux, F., *et al.* (2016) Small molecule proteostasis regulators that reprogram the ER to reduce extracellular protein aggregation. *eLife* **5**, e15550

50. Braak, H., and Braak, E. (1991) Neuropathological staging of Alzheimer-related changes. *Acta Neuropathol.* **82**, 239–259

51. Braak, H., and Braak, E. (1996) Evolution of the neuropathology of Alzheimer's disease. *Acta Neurol. Scand. Suppl.* **165**, 3–12

52. Goedert, M., Spillantini, M. G., Cairns, N. J., and Crowther, R. A. (1992) Tau proteins of Alzheimer paired helical filaments: abnormal phosphorylation of all six brain isoforms. *Neuron* **8**, 159–168

53. Hitt, B. D., Vaquer-Alicea, J., Manon, V. A., Beaver, J. D., Kashmer, O. M., Garcia, J. N., *et al.* (2021) Ultrasensitive tau biosensor cells detect no seeding in Alzheimer's disease CSF. *Acta Neuropathol. Commun.* **9**, 99

54. Seidler, P. M., Boyer, D. R., Rodriguez, J. A., Sawaya, M. R., Cascio, D., Murray, K., *et al.* (2018) Structure-based inhibitors of tau aggregation. *Nat. Chem.* **10**, 170–176

55. Nativio, R., Lan, Y., Donahue, G., Sidoli, S., Berson, A., Srinivasan, A. R., *et al.* (2020) An integrated multi-omics approach identifies epigenetic alterations associated with Alzheimer's disease. *Nat. Genet.* **52**, 1024–1035

56. Mizuno, Y., Abolhassani, N., Mazzei, G., Sakumi, K., Saito, T., Saido, T. C., *et al.* (2021) MUTYH actively contributes to microglial activation and impaired neurogenesis in the pathogenesis of Alzheimer's disease. *Oxid Med. Cell Longev.* **2021**, 8635088

57. Takigawa, H., Kitayama, M., Wada-Isoe, K., Kowa, H., and Nakashima, K. (2016) Prevalence of progressive supranuclear palsy in yonago: change throughout a decade. *Brain Behav.* **6**, e00557

58. Schrag, A., Ben-Shlomo, Y., and Quinn, N. P. (1999) Prevalence of progressive supranuclear palsy and multiple system atrophy: a cross-sectional study. *Lancet* **354**, 1771–1775

59. Viscidi, E., Litvan, I., Dam, T., Juneja, M., Li, L., Krzywy, H., *et al.* (2021) Clinical features of patients with progressive supranuclear palsy in an US insurance claims database. *Front. Neurol.* **12**, 571800

60. Bertolotti, A., Zhang, Y., Hendershot, L. M., Harding, H. P., and Ron, D. (2000) Dynamic interaction of BiP and ER stress transducers in the unfolded-protein response. *Nat. Cell Biol.* **2**, 326–332

61. Hashimoto, S., Ishii, A., Kamano, N., Watamura, N., Saito, T., Ohshima, T., *et al.* (2018) Endoplasmic reticulum stress responses in mouse models of Alzheimer's disease: overexpression paradigm versus knockin paradigm. *J. Biol. Chem.* **293**, 3118–3125

62. Pitera, A. P., Asuni, A. A., O'Connor, V., and Deinhardt, K. (2019) Pathogenic tau does not drive activation of the unfolded protein response. *J. Biol. Chem.* **294**, 9679–9688

63. Hoozemans, J. J., Veerhuis, R., Van Haastert, E. S., Rozemuller, J. M., Baas, F., Eikelenboom, P., *et al.* (2005) The unfolded protein response is activated in Alzheimer's disease. *Acta Neuropathol. (Berl)* **110**, 165–172

64. Stutzbach, L. D., Xie, S. X., Naj, A. C., Albin, R., Gilman, S., Group, P. S. P. G. S., *et al.* (2013) The unfolded protein response is activated in disease-affected brain regions in progressive supranuclear palsy and Alzheimer's disease. *Acta Neuropathol. Commun.* **1**, 31

65. Bruch, J., Xu, H., Rosler, T. W., De Andrade, A., Kuhn, P. H., Lichtenthaler, S. F., *et al.* (2017) PERK activation mitigates tau pathology *in vitro* and *in vivo*. *EMBO Mol. Med.* **9**, 371–384

66. Li, R., Li, Y., Kristiansen, K., and Wang, J. (2008) Soap: short oligonucleotide alignment program. *Bioinformatics* **24**, 713–714

67. Kim, D., Langmead, B., and Salzberg, S. L. (2015) Hisat: a fast spliced aligner with low memory requirements. *Nat. Met.* **12**, 357–360

68. Langmead, B., and Salzberg, S. L. (2012) Fast gapped-read alignment with Bowtie 2. *Nat. Met.* **9**, 357–359

69. Li, B., and Dewey, C. N. (2011) Rsem: accurate transcript quantification from RNA-seq data with or without a reference genome. *BMC Bioinform.* **12**, 323

70. Love, M. I., Huber, W., and Anders, S. (2014) Moderated estimation of fold change and dispersion for RNA-seq data with DESeq2. *Genome Biol.* **15**, 550